ChemComm

COMMUNICATION

View Article Online
View Journal | View Issue

Cite this: *Chem. Commun.*, 2022, **58**, 11167

Received 20th July 2022,
Accepted 7th September 2022

DOI: 10.1039/d2cc03979f

rsc.li/chemcomm

Bridging oxygen atoms in trigonal prism units driven strong second-harmonic-generation efficiency in $Sr_3Ge_2O_4Te_3$†

Mengran Sun,[abc] Wenhao Xing,[d] Ming-Hsien Lee *[e] and Jiyong Yao *[ab]

Herein, a novel IR NLO oxytelluride $Sr_3Ge_2O_4Te_3$ was successfully designed and synthesized through a "partial O-to-Te substitution" strategy. Compared with the parent oxide, $Sr_3Ge_2O_4Te_3$ not only successfully achieves a phase-matchability transition (from NPM to PM), but also greatly improves the linear and NLO performances, including a wide band gap (2.26 eV), strong SHG response (1.3 × $AgGaSe_2$) and large optical anisotropy (Δn = 0.152@2090 nm). The analyses of the structure–property relationship and SHG-density indicate that the bridging oxygen in the [O_3Ge–O–$GeTe_3$] prism unit plays the most important role in the multiplication SHG effect. This work provides some insights into the design and exploration of novel IR NLO materials.

Infrared (IR) nonlinear optical (NLO) materials are of great interest due to their ability to generate coherent tunable lasers in the IR region (2–20 μm), which are widely used in medical diagnostics, laser guidance, and laser atmospheric communication.[1] To date, only $AgGaQ_2$ (Q = S, Se) and $ZnGeP_2$ have been used as commercially available IR NLO crystals.[2] However, the intrinsic drawbacks of these materials limit their applications in high-power lasers.[3] In general, as a potential IR NLO material, the following requirements should be satisfied: (1) non-centrosymmetric (NCS) structure; (2) large second-harmonic-generation (SHG) coefficient (d_{eff}); (3) sufficient optical anisotropy (Δn); (4) wide band gap (E_g).[4] However, these parameters are interrelated, and are difficult to regulate and control simultaneously. Therefore, how to balance these parameters in a crystal structure remains a huge challenge in modern laser technology and science.

In the past few decades, abundant efforts have been made to obtain NLO materials with well-balanced properties.[5] At present, a reasonable strategy has been proposed—to construct two different anions into one compound through molecular design, which may achieve breakthroughs in material properties. For example, oxides and halides have small SHG coefficients but large band gaps, while chalcogenides (especially tellurides) do the opposite.[6] Combining these two anions into one crystal (heteroanionic inorganic compound) has the potential to simultaneously satisfy a larger SHG response and wider band gap.[5a,7] An effective approach to obtain heteroanions is to select a unit/compound as the structural template, and then employ an equivalent/aliovalent anion substitution strategy.[8] For example, the substitution of oxygen atoms in $[BO_4]^{5-}$ or $[PO_4]^{4-}$ tetrahedra with highly electronegative F atoms, forms mixed oxyfluoride units $[BO_{4-x}F_x]^{(5-x)-}$ (x = 1, 2, 3) and $[PO_{4-x}F_x]^{(4-x)-}$ (x = 1, 2), which not only expand the transparency of the DUV range but also enhance the SHG response.[9]

Based on the understanding of the structure–property relationship, the smaller electronegativity of the Te atom may be the underlying reason why tellurides have larger electronic polarization than sulfides and selenides do.[6b,10] In addition, the long-wave transparency cut-off edges of tellurides may be red-shifted compared to the aforementioned compounds, resulting in wider IR transmission ranges.[3b] For example, $AgGaTe_2$ exhibits a larger SHG coefficient (d_{eff} = 77 pm V^{-1}) and a wider IR transmission range (0.61–23 μm) than $AgGaS_2$ (d_{36} = 13 pm V^{-1}, 0.47–13 μm) and $AgGaSe_2$ (d_{36} = 36 pm V^{-1}, 0.71–18.3 μm) do;[11] $CsCd_4In_5Te_{12}$ possesses a strong SHG response (SHG: 9 × AGS) than $CsCd_4In_5S_{12}$ (SHG: 1.1 × AGS) does.[12] Furthermore, the chain-like structures that tellurides tend to form favor sufficient birefringence to ensure phase matching.[13] Therefore, metal tellurides have been considered as one of the promising candidates for exploring IR NLO

[a] Beijing Center for Crystal Research and Development, Key Lab of Functional Crystals and Laser Technology, Technical Institute of Physics and Chemistry, Chinese Academy of Sciences, Beijing 100190, P. R. China
[b] Center of Materials Science and Optoelectronics Engineering, University of Chinese Academy of Sciences, Beijing 100049, P. R. China
[c] University of Chinese Academy of Sciences, Beijing 100049, P. R. China
[d] Institute of Chemical Materials, China Academy of Engineering Physics, Mianyang 621900, P. R. China
[e] Department of Physics, Tamkang University, Tamsui, New Tapei 25137, Taiwan. E-mail: mhslee@mail.tku.edu.tw

† Electronic supplementary information (ESI) available: Experimental details, characterization, and crystallographic data. CCDC 2182403. For ESI and crystallographic data in CIF or other electronic format see DOI: https://doi.org/10.1039/d2cc03979f

materials. However, the narrow band gap of conventional tellurides seriously hinders the applications of telluride materials to achieve high laser output, which is caused by the higher energy level of Te atoms. Therefore, oxytellurides, which might inherit the performance advantages of oxides and tellurides, are regarded as a new class of IR NLO materials.

Melilite-type oxides with the general formula $AE_2M^{II}M^{IV}{}_2O_7$ (AE = Ba, Sr, Eu; M^{II} = Mg, Zn, Cd, Mn, Cu; M^{IV} = Si, Ge, Sn) are $\chi^{(2)}$-active nonlinear multifunctional crystals with large bandgaps exhibiting diverse physical properties.[14] However, most of them exhibit weak SHG response or NPM features in the UV-vis range, which seriously hinders their further applications.[14b,15] In this work, using the melilite-type crystal $Sr_2ZnGe_2O_7$ as the structural template, the "partial O-to-Te substitution" strategy was implemented to yield mixed-anion asymmetric building blocks (ABBs), which is expected to achieve a balance between strong NLO response, large birefringence, and wide band gap. As expected, a new IR NLO material $Sr_3Ge_2O_4Te_3$ with balanced-properties was successfully obtained. Herein, the crystal structure, NLO properties, and theoretical calculations of $Sr_3Ge_2O_4Te_3$ were systemically studied.

$Sr_3Ge_2O_4Te_3$ was synthesized by high temperature solid-state reaction (ESI†) and yellow-brown block-like crystals were obtained. The XRD pattern indicated the purity of the polycrystalline powder (Fig. 2a). The SEM and EDX mapping results illustrate that the Sr, Ge, and Te elements are uniformly distributed in the crystal and approximately in the molar ratio of 3 : 2 : 3 (Fig. S3, ESI†). Moreover, the calculation of bond valence sums (BVSs) indicates the desirable valence states Sr^{2+}, Ge^{4+}, O^{2-}, and Te^{2-} (Table S2, ESI†). In addition, the differential scanning calorimetry (DSC) curve shows that the melting point of $Sr_3Ge_2O_4Te_3$ is 915 °C (Fig. S8, ESI†). And the XRD pattern after-melting indicates that the residues are SrTe, GeTe and SrO_2, which demonstrates that $Sr_3Ge_2O_4Te_3$ has a non-congruent melting behavior (Fig. 2a).

$Sr_3Ge_2O_4Te_3$ crystallizes in the space group *R*3*m* (No. 160) (Table S1, ESI†). In the asymmetric unit, there are one crystallographically independent Sr atoms, two Ge atoms, two O atoms (O2 has a 33.3% occupancy rate), and one Te atom (Fig S4, ESI†). As shown in Fig. 1d, $Sr_3Ge_2O_4Te_3$ features parallel clusters of the zero-dimensional (0D) $[Ge_2O_4Te_3]^{6-}$ units along the *b* axis. These 0D clusters consist of a $[Ge(1)O_4]$ tetrahedron and a $[Ge(2)OTe_3]$ tetrahedron by sharing O(2) atoms (Fig. 1g). Then, the Sr^{2+} cations located at the interstices built by these clusters (Fig. 1b). Moreover, the Sr atoms are coordinated with five Te atoms and three O atoms to form an irregular $[SrO_3Te_5]$ polyhedron (Fig. S6b, ESI†).

Notably, comparing the structures of $Sr_3Ge_2O_4Te_3$ and $Sr_2ZnGe_2O_7$ can illustrate their structural evolution. Firstly, all the Zn^{2+} cations in $Sr_2ZnGe_2O_7$ are replaced with equivalent Sr^{2+} cations, which is beneficial to reduce the structural dimensions and widen the band gap. In addition, $Sr_3Ge_2O_4Te_3$ is derived from the partial substitution of Te^{2-} anions for the O^{2-} anions in $Sr_2ZnGe_2O_7$ (Fig. 1a and b). Therefore, $Sr_2ZnGe_2O_7$ with 2D $^2_\infty[ZnGe_2O_7]^{4-}$ layers is transformed into $Sr_3Ge_2O_4Te_3$ with 0D $[Ge_2O_4Te_3]^{6-}$ clusters (Fig. 1c and d). More importantly, the arrangement of $[Ge_2O_7]$ dimers in $Sr_2ZnGe_2O_7$ is disordered (the ZnO_4 tetrahedra are not shown for clarity), while all of the 0D $[Ge_2O_4Te_3]^{6-}$ clusters in $Sr_3Ge_2O_4Te_3$ are aligned in a parallel manner (Fig. 1e and f). On the one hand, the anisotropic coordination in the mixed-anion $[GeOTe_3]$ unit is beneficial to enhance the dipole moment of individual polyhedra. On the other hand, the size (volume) difference between $[GeO_4]$ and $[GeOTe_3]$ is not significant, so as not to cause alternating (space-complemental) packing. This then leaves the dipole electric field to make these units pointing in the same direction, adding up the SHG contribution. Notably, $Sr_2ZnGe_2O_7$

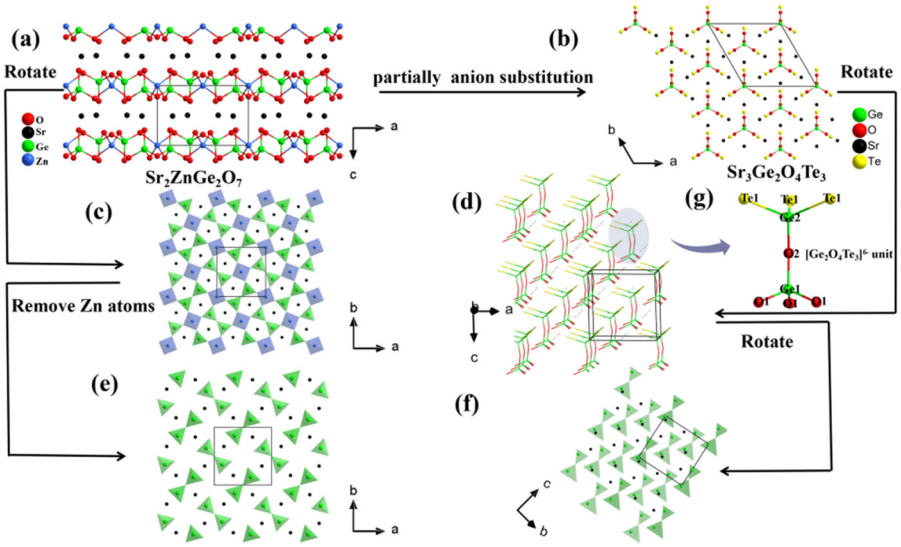

Fig. 1 Crystal structural evolution from $Sr_2ZnGe_2O_7$ to $Sr_3Ge_2O_4Te_3$. (a) The crystal structure of $Sr_2ZnGe_2O_7$ along the *b* axis; (b) the crystal structure of $Sr_3Ge_2O_4Te_3$ along the *c* axis; (c) the $^2_\infty[ZnGe_2O_7]^{4-}$ layer constructed by a corner-sharing $[Ge_2O_7]$ dimer and $[ZnO_4]$ tetrahedron; (d) the stick model of $Sr_3Ge_2O_4Te_3$ along the *b* axis; (e) the $^2_\infty[ZnGe_2O_7]^{4-}$ layer removes the Zn atoms; (f) the arrangement of $[Ge_2O_4Te_3]^{6-}$ units along the *a* axis; (g) the $[Ge_2O_4Te_3]^{6-}$ unit.

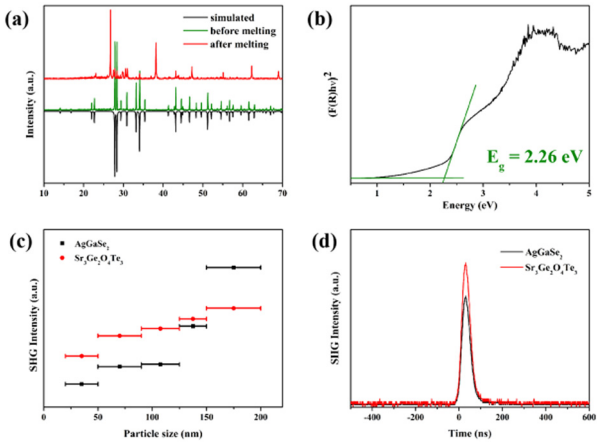

Fig. 2 (a) Experimental and simulated powder XRD patterns of $Sr_3Ge_2O_4Te_3$; (b) the UV-vis-NIR diffuse reflectance spectrum of $Sr_3Ge_2O_4Te_3$; (c) phase-matching curve of $Sr_3Ge_2O_4Te_3$; (d) SHG signal of $Sr_3Ge_2O_4Te_3$ in the size range of 90–125 μm. $AgGaSe_2$ was used as the reference.

possesses [GeO_4] and [ZnO_4] tetrahedra with Ge–O and Zn–O bonds distances ranging from 1.685(6) to 1.819(7) Å and 1.883(6) Å, respectively.[14b] Compared with $Sr_2ZnGe_2O_7$, the Ge(2) atom in $Sr_3Ge_2O_4Te_3$ is surrounded by three Te atoms and one O atom forming the distorted [Ge(2)OTe_3] tetrahedron with Ge–O and Ge–Te bonds of 1.787(26) Å and 2.545(1) Å, respectively (Fig. S5, ESI†), and the bond angles range from 95.0(8) to 116.0(3)° (Table S3, ESI†). And the [SrO_8] unit is replaced by a [SrO_3Te_5] unit with Sr–O bonds lengths ranging from 2.474(9) to 2.602(6) Å and the Sr–Te bonds lengths ranging from 3.500(2) to 3.607(2) Å (Fig. S6, ESI†).

The UV-vis-NIR diffuse reflectance spectrum of $Sr_3Ge_2O_4Te_3$ shows an experimental E_g of 2.26 eV using the Kubelka–Munk equation (Fig. 2b). This value is larger than those of several oxytellurides.[16] The IR and Raman spectra of $Sr_3Ge_2O_4Te_3$ are given in Fig. S7 (ESI†). The absorption peaks located at 725 and 837 cm^{-1} in the IR spectrum and the peak at 768 cm^{-1} in the Raman spectrum can be attributed to the vibration of Ge–O bonds, and are consistent with those in $BaGeOSe_2$ and $Sr_3Ge_2O_4Se_3$.[17] The peak at 3460 cm^{-1} in the IR spectrum corresponds to the vibration of the O–H bonds.[18]

The powder SHG intensities of $Sr_3Ge_2O_4Te_3$ were measured using a 2.09 μm laser (Q-switched Ho:Tm:-Cr:YAG) as fundamental light based on a Kurtz–Perry technique.[19] Meanwhile, the NLO material $AgGaSe_2$ with similar particle sizes was used as the benchmark. Clearly, the SHG intensities of $Sr_3Ge_2O_4Te_3$ increase with the increase of the particle size, and then reach a plateau at the maximum value after a certain particle size (Fig. 2c), suggesting a Type-I phase-matching behavior. The good phase-matching ability is crucial for NLO materials, which can significantly improve the conversion efficiency of frequency-doubled light. Remarkably, the title compound exhibits a strong SHG response of 1.3 times that of benchmark $AgGaSe_2$ at a particle size of 90–125 μm (Fig. 2d). In addition, the laser damage thresholds (LDTs) of $Sr_3Ge_2O_4Te_3$ and $AgGaSe_2$ were also estimated. The LDT of $Sr_3Ge_2O_4Te_3$ was determined to be 7.96 MW cm^{-2}, which is about 0.8 times that of AGSe (9.95 MW cm^{-2}).

To further reveal the structure–activity relationship of $Sr_3Ge_2O_4Te_3$, the first-principles calculations based on DFT were performed using the CASTEP package.[20] The electronic band structure of $Sr_3Ge_2O_4Te_3$ is depicted in Fig. 3a, which illustrates that $Sr_3Ge_2O_4Te_3$ is a direct band gap compound with a calculated E_g of 1.718 eV. The total and partial density of states (DOS) are shown in Fig. 3c, the top region of the valence bands (VBs) is primarily composed of Te 5p and O(1) 2p orbitals, while the bottom region of the conduction bands (CBs) mainly originates from Te 5p and Ge(2) 4s orbitals. Thus, the [$GeTe_3$] units are the main source of the band gap of $Sr_3Ge_2O_4Te_3$.

Furthermore, detailed calculations for the NLO coefficient and birefringence of $Sr_3Ge_2O_4Te_3$ were performed. Optical property calculations were carried out for the determined (idealized) crystal structure and fully (cell-volume and ion positions) relaxed one, and the results are given in Tables S4 and S5 (ESI†), respectively. Taking the results of the first calculation as an example, the NLO coefficient of $Sr_3Ge_2O_4Te_3$ (d_{15} = −8.78 pm V^{-1}) exhibits an order of magnitude increase compared with that of $Sr_2ZnGe_2O_7$ (d_{eff} = 0.51 pm V^{-1}). In addition, the birefringence of $Sr_3Ge_2O_4Te_3$ was calculated to be 0.152@2090 nm (Fig. 3b), which is approximately 6 times that of $Sr_2ZnGe_2O_7$ (Δn = 0.025@1064 nm). It is obvious that the large birefringence of the crystal originated from dielectric anisotropy of rod-like anion-units lined-up in parallel. Besides, the SHG-density[21] maps of virtual-electron occupied (veocc) and virtual-hole unoccupied (vhunocc) states are used to visually demonstrate the contribution of different atoms or groups to the SHG response (Note: Inverse rainbow drawing for densities above half the intensity). As shown in Fig. 4, the largest d_{ij} component mainly comes from the non-bonding group VI elements (O and Te) of fully lined up trigonal prism molecular units O_3Ge–O–$GeTe_3$. And it partly comes from the cup-side of the empty orbital of Ge centered in the [$GeOTe_3$] unit and the empty orbital on the bridging oxygen between the [$GeTe_3$] and [GeO_3] subunits, of which the latter is likely most important because there is an "on-site" transition between SHG-related occupied and unoccupied states.

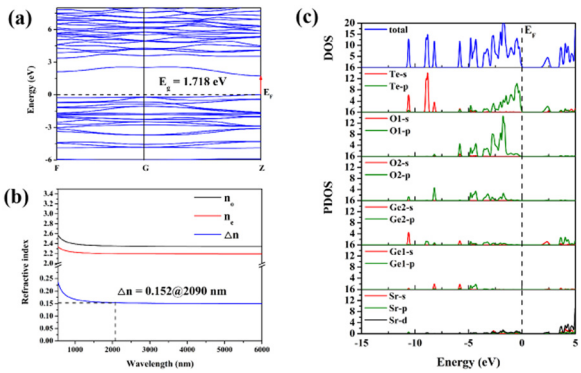

Fig. 3 (a) Calculated electronic band structure of $Sr_3Ge_2O_4Te_3$. (b) Calculated refractive dispersion curve of $Sr_3Ge_2O_4Te_3$. (c) Total and partial density of states of $Sr_3Ge_2O_4Te_3$.

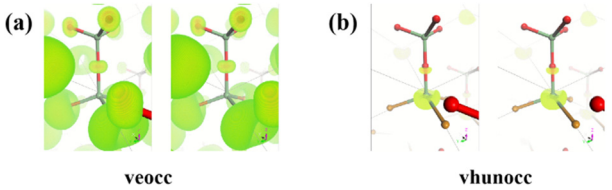

Fig. 4 Stereo pair (cross-eyes) of the virtual-electron occupied (veocc) (a), and virtual-hole unoccupied (vhunocc) (b) SHG-density of the largest d_{ij} component.

In summary, a new IR NLO crystal $Sr_3Ge_2O_4Te_3$ was successfully designed and synthesized by a "partial O-to-Te substitution" strategy. It crystallizes in the *R3m* space group and features a unique $[Ge_2O_4Te_3]$ molecular unit. Notably, $Sr_3Ge_2O_4Te_3$ exhibits well-balanced properties, including a wide band gap, strong SHG response, and large optical anisotropy. From the results and analysis of detailed theoretical studies, the bridging oxygen in a polar chemical environment sandwiched between $[GeO_3]$ and $[GeTe_3]$ plays the most important role in the enhanced SHG effect of $Sr_3Ge_2O_4Te_3$, and the perfect alignment of all $[Ge_2Te_3O_4]$ units in parallel within the entire crystal achieves a high SHG effect. To the best of our knowledge, this is a new type of mechanism to achieve simultaneously large SHG and large birefringence by using a structured form of a single anion-group unit. More importantly, the molecular polar trigonal prism $[Ge_2O_4Te_3]$ consisting of two tetrahedral units in an eclipse manner could open up a new family of building blocks for efficient SHG crystals.

This work is supported by the National Natural Science Foundation of China (Grant No. 22175190 and 51890862).

Conflicts of interest

There are no conflicts to declare.

Notes and references

1 (*a*) L. Byer Robert, *Science*, 1988, **239**(4841), 742–747; (*b*) U. Keller, *Nature*, 2003, **424**(6950), 831–838; (*c*) G. Li, Z. Yang, J. Li and S. Pan, *Chem. Commun.*, 2020, **56**(78), 11565–11576; (*d*) Z. Li, Y. Yang, Y. Guo, W. Xing, X. Luo, Z. Lin, J. Yao and Y. Wu, *Chem. Mater.*, 2019, **31**(3), 1110–1117; (*e*) Z. Li, X. Jiang, M. Zhou, Y. Guo, X. Luo, Y. Wu, Z. Lin and J. Yao, *Inorg. Chem.*, 2018, **57**(17), 10503–10506.
2 (*a*) T. Elsaesser, A. Seilmeier, W. Kaiser, P. Koidl and G. Brandt, *Appl. Phys. Lett.*, 1984, **44**(4), 383–385; (*b*) T. Bai, S. Xing, C. Li, Z. Shi and S. Feng, *Chem. Commun.*, 2016, **52**(55), 8581–8584; (*c*) K. Masumoto, S. Isomura and W. Goto, *J. Phys. Chem. Solids*, 1966, **27**(11), 1939–1947.
3 (*a*) M. Y. Ran, Z. Ma, H. Chen, B. Li, X. T. Wu, H. Lin and Q. L. Zhu, *Chem. Mater.*, 2020, **32**(13), 5890–5896; (*b*) X. Luo, Z. Li, Y. Guo, J. Yao and Y. Wu, *J. Solid State Chem.*, 2019, **270**, 674–687.
4 (*a*) M. Y. Ran, S. H. Zhou, B. Li, W. Wei, X. T. Wu, H. Lin and Q. L. Zhu, *Chem. Mater.*, 2022, **34**(8), 3853–3861; (*b*) W. Wang, D. Mei, F. Liang, J. Zhao, Y. Wu and Z. Lin, *Coord. Chem. Rev.*, 2020, **421**, 213444; (*c*) S. P. Guo, Y. Chi and G. C. Guo, *Coord. Chem. Rev.*, 2017, **335**, 44–57; (*d*) P. Gong, F. Liang, L. Kang, X. Chen, J. Qin, Y. Wu and Z. Lin, *Coord. Chem. Rev.*, 2019, **380**, 83–102.
5 (*a*) M. Sun, X. Zhang, C. Li, W. Liu, Z. Lin and J. Yao, *J. Mater. Chem. C*, 2022, **10**(1), 150–159; (*b*) Z. Li, S. Zhang, Z. Huang, L. D. Zhao, E. Uykur, W. Xing, Z. Lin, J. Yao and Y. Wu, *Chem. Mater.*, 2020, **32**(7), 3288–3296; (*c*) W. Xing, N. Wang, C. Tang, C. Li, Z. Lin, J. Yao, W. Yin and B. Kang, *J. Mater. Chem. C*, 2021, **9**(3), 1062–1068; (*d*) W. Xing, C. Tang, N. Wang, C. Li, E. Uykur, J. Wu, Z. Lin, J. Yao, W. Yin and B. Kang, *Adv. Opt. Mater.*, 2021, **9**(15), 2100563; (*e*) X. Huang, S. H. Yang, X. H. Li, W. Liu and S. P. Guo, *Angew. Chem. Int. Ed.*, 2022, **61**, e202206791 (*Angew. Chem.*, 2022, **134**, e202206791); (*f*) M. M. Chen, S. H. Zhou, W. Wei, M. Y. Ran, B. Li, X. T. Wu, H. Lin and Q. L. Zhu, *ACS Mater. Lett.*, 2022, 1264–1269.
6 (*a*) M. Mutailipu, Z. Xie, X. Su, M. Zhang, Y. Wang, Z. Yang, M. R. S. A. Janjua and S. Pan, *J. Am. Chem. Soc.*, 2017, **139**(50), 18397–18405; (*b*) M. Y. Ran, Z. Ma, X. T. Wu, H. Lin and Q. L. Zhu, *Inorg. Chem. Front.*, 2021, **8**(22), 4838–4845; (*c*) W. Liu, X. Liu, X. Meng, C. Li, M. Sun, Z. Lin and J. Yao, *J. Alloys Compd.*, 2022, **902**, 163832; (*d*) M. Zhou, Y. Yang, Y. Guo, Z. Lin, J. Yao, Y. Wu and C. Chen, *Chem. Mater.*, 2017, **29**(18), 7993–8002.
7 (*a*) R. Wang, Y. Guo, X. Zhang, Y. Xiao, J. Yao and F. Huang, *Inorg. Chem.*, 2020, **59**(14), 9944–9950; (*b*) B. W. Liu, H. Y. Zeng, X. M. Jiang, G. E. Wang, S. F. Li, L. Xu and G. C. Guo, *Chem. Sci.*, 2016, **7**(9), 6273–6277; (*c*) P. Yu, L. J. Zhou and L. Chen, *J. Am. Chem. Soc.*, 2012, **134**(4), 2227–2235.
8 (*a*) M. Ran, Z. Ma, H. Chen, B. Li, X. Wu, H. Lin and Q. Zhu, *Chem. Mater.*, 2020, **32**(13), 5890–5896; (*b*) B. Liu, X. Jiang, G. Wang, H. Zeng, M. Zhang, S. Li, W. Guo and G. Guo, *Chem. Mater.*, 2015, **27**(24), 8189–8192.
9 (*a*) H. Qiu, F. Li, C. Jin, J. Lu, Z. Yang, S. Pan and M. Mutailipu, *Chem. Commun.*, 2022, **58**(37), 5594–5597; (*b*) L. Xiong, J. Chen, J. Lu, C. Y. Pan and L. M. Wu, *Chem. Mater.*, 2018, **30**(21), 7823–7830; (*c*) M. Mutailipu and S. Pan, *Angew. Chem., Int. Ed.*, 2020, **59**(46), 20302–20317; (*d*) B. Zhang, G. Han, Y. Wang, X. Chen, Z. Yang and S. Pan, *Chem. Mater.*, 2018, **30**(15), 5397–5403; (*e*) B. Zhang, G. Shi, Z. Yang, F. Zhang and S. Pan, *Angew. Chem., Int. Ed.*, 2017, **56**(14), 3916–3919.
10 M. Sun, X. Zhang, W. Xing, Z. Li, W. Liu, Z. Lin, W. Yin and J. Yao, *Inorg. Chem.*, 2021, **60**(19), 14793–14802.
11 L. Bai, Z. Lin, Z. Wang, C. Chen and M.-H. Lee, *J. Chem. Phys.*, 2004, **120**(18), 8772–8778.
12 (*a*) H. Lin, Y. Liu, L. J. Zhou, H. J. Zhao and L. Chen, *Inorg. Chem.*, 2016, **55**(9), 4470–4475; (*b*) Y. Wang, R. Wang, X. Che, F. Liang, M. Luo, Y. Tang, Y. Cao and F. Huang, *J. Mater. Chem. C*, 2022, **10**(13), 5183–5189.
13 S. A. Avanesov, D. V. Badikov, V. V. Badikov, V. L. Panyutin, V. Petrov, G. S. Shevyrdyaeva, A. A. Martynov and K. V. Mitin, *J. Alloys Compd.*, 2014, **612**, 386–391.
14 (*a*) C. L. Teske, *Z. Anorg. Allg. Chem.*, 1985, **531**(12), 52–60; (*b*) P. Becker, P. Held, J. Liebertz and L. Bohatý, *Cryst. Res. Technol.*, 2009, **44**(6), 603–612; (*c*) T. Endo, Y. Doi, M. Wakeshima, K. Suzuki, Y. Matsuo, K. Tezuka, T. Ohtsuki, Y. J. Shan and Y. Hinatsu, *Inorg. Chem.*, 2017, **56**(5), 2459–2466; (*d*) W. Zhang, J. Feng, F. Lu, A. J. Fernández-Carrión, H. Fu and X. Kuang, *J. Mater. Chem. A*, 2021, **9**(38), 22064–22071; (*e*) C. Yin, Z. Yu, L. Shu, L. Liu, Y. Chen and C. Li, *J. Adv. Ceram.*, 2021, **10**(1), 108–119.
15 Y. Chi, H. G. Xue and S. P. Guo, *Dalton Trans.*, 2018, **47**(38), 13434–13441.
16 D. Song, G. Guélou, T. Mori, M. Ochi, K. Kuroki, H. Fujihisa, Y. Gotoh, Y. Iwasa, H. Eisaki and H. Ogino, *J. Mater. Chem. C*, 2018, **6**(45), 12260–12266.
17 (*a*) B. W. Liu, X. M. Jiang, G. E. Wang, H. Y. Zeng, M. J. Zhang, S. F. Li, W. H. Guo and G. C. Guo, *Chem. Mater.*, 2015, **27**(24), 8189–8192; (*b*) W. Xing, P. Fang, N. Wang, Z. Li, Z. Lin, J. Yao, W. Yin and B. Kang, *Inorg. Chem.*, 2020, **59**(22), 16716–16724.
18 Z. X. Tian, X. Zhang, C. L. Liu, Q. G. Meng, Z. F. Du and J. Yan, *Anal. Lett.*, 2020, **53**(13), 2034–2046.
19 S. Kurtz and T. Perry, *J. Appl. Phys.*, 1968, **39**(8), 3798–3813.
20 M. D. Segall, P. J. D. Lindan, M. J. Probert, C. J. Pickard, P. J. Hasnip, S. J. Clark and M. C. Payne, *J. Phys.: Condens. Matter*, 2002, **14**(11), 2717–2744.
21 C.-H. Lo, Master degree thesis (Supervised by Lee, M.-H.), Tamkang University, 2005, p. 29.

